Photocatalytically recovering hydrogen energy from wastewater treatment using MoS$_2$ @TiO$_2$ with sulfur/oxygen dual-defect

Yaoyao Wu [a], Xiaotao Chen [a], Jiachun Cao [b], Yuqing Zhu [a], Wenjing Yuan [a], Zhuofeng Hu [a], Zhimin Ao [b], Gary W. Brudvig [c,*], Fenghui Tian [d], Jimmy C. Yu [e], Chuanhao Li [a,*]

[a] Guangdong Provincial Key Laboratory of Environmental Pollution Control and Remediation Technology, School of Environmental Science and Engineering, Sun Yat-sen University, Guangzhou 510006, China
[b] Guangdong Key Laboratory of Environmental Catalysis and Health Risk Control, Guangzhou Key Laboratory Environmental Catalysis and Pollution Control, School of Environmental Science and Engineering, Institute of Environmental Health and Pollution Control, Guangdong University of Technology, Guangzhou 510006, China
[c] Yale Energy Sciences Institute and Department of Chemistry, Yale University, New Haven, Connecticut 06520–8107, United States
[d] Institute of Computational Science and Engineering, State Key Laboratory of Bio-Fibers and Eco-Textiles & College of Chemistry and Chemical Engineering & College of Environmental Science and Engineering, Qingdao University, Qingdao 266071, China
[e] Department of Chemistry, The Chinese University of Hong Kong, New Territories, Hong Kong, Shatin, China

ARTICLE INFO

ABSTRACT

Photocatalysis is a promising technology for energy and environment applications. Herein, a dual-defect heterojunction system of TiO$_2$ hierarchical microspheres with oxygen vacancies modified with ultrathin MoS$_{2-x}$ nanosheets (MoS$_{2-x}$ @TiO$_2$-OV) is designed for simultaneously degrading pollutants and evolving hydrogen. MoS$_{2-x}$ @TiO$_2$-OV exhibits a dramatically enhanced photocatalytic activity with a H$_2$ evolution rate of 2985.16 μmol g^{-1}h^{-1}. In treating the simulated pharmaceutical wastewater, MoS$_{2-x}$ @TiO$_2$-OV is capable of purifying various refractory contaminants, with the highest H$_2$ evolution rate of 41.59 μmol g^{-1}h^{-1} during enrofloxacin degradation. While treating the simulated coking wastewater, the catalyst achieves a H$_2$ evolution rate of 102.72 μmol g^{-1}h^{-1} and a mineralization rate of 50%. Computational studies suggest that the dual-defect is superior for the adsorption of H* and producing·OH ('dual-defect boosted dual-function'). Also, the dual-defect sites significantly boosted the charge-carrier separation and transfer efficiencies. This work highlights the crucial role of defect engineering to develop the energy-recovering wastewater treatment approaches.

1. Introduction

Simultaneous hydrogen energy recovery in combination with degradation of refractory organic pollutants is an attractive and promising solution to tackle energy and environmental problems [1–4]. In a typical photocatalytic H$_2$ evolution process, researchers commonly focus on the reaction mechanism related to the reducing capability of photogenerated electrons for H$_2$ generation, but the crucial role of holes is often overlooked. To initiate the redox reactions, currently, the common approach is to use noble metals, such as platinum, as the hydrogen evolution reaction (HER) co-catalyst and a highly toxic sacrificial reagent, such as methanol, to quench the photo-generated holes. However, the incorporation of toxic or expensive substituents in the photocatalytic H$_2$ evolution systems has greatly restricted the potential for practical applications of this technology [5–7]. Therefore, it is

urgent to seek alternative cost-effective co-catalysts and sacrificial reagents. There are growing concerns for the discharge of pharmaceutical [8,9] and coking wastewater [10,11] with biologically refractory organic contaminants. While typically seen as pollutants (e.g. enrofloxacin, phenol, pyridine, indole and quinoline) [12–14], such organic compounds contained in the wastewater carry tremendous chemical energy. Thus, it would be beneficial to purify the wastewater while simultaneously conducting energy conversion.

To exploit highly efficient and noble-metal-free cocatalysts to facilitate the development of photocatalytic hydrogen evolution (PHE), cost-effective and stable transition metal dichalcogenides (TMDs) can be promising alternatives [15]. As a model TMD for HER catalysis, MoS$_2$ possesses superior properties, such as good electrical conductivity in the layer, prolonged stability, and optimal thermodynamics in stabilizing the intermediate species [16]. However, the HER activity was hindered

by the low conductivity between layers and the limited active sites on the basal plane [17,18]. Tremendous work has been devoted to enhancing the HER catalytic activity of MoS_2. For example, Xie et al. developed a method to add a controllable amount of oxygen (O) dopants into 2D MoS_2 nanosheets to effectively improve their intrinsic conductivity [19]. In addition, a recent report shows that MoS_2 nanosheets with abundant sulfur (S)-defect sites coated on nitrogen (N)-doped ZnO NRs can remarkably boost the H_2 evolution activity [20]. Thus, maximizing the exposed unsaturated S defects on the edges can significantly promote HER activity.

To overcome the issues of using highly toxic and expensive organic compounds as sacrificial agents, an alternative approach is to utilize refractory and harmful organic contaminants as electron donors. If photogenerated holes can efficiently react with the organic pollutants at the surface/interface, the electron-hole recombination rate can be suppressed and the performance of the H_2 evolution half-reaction will be improved. In terms of thermodynamics, TiO_2 with suitable energy-band positions can be employed to trigger the complementary redox reactions, but the applications of TiO_2 suffer from the limited visible light adsorption and the weak surface interaction with organic pollutants [21]. To overcome the aforementioned issues, the introduction of oxygen vacancies (OVs) has emerged as a prevalent strategy to regulate the electronic band structure and intrinsic active sites of TiO_2 [22,23]. For example, Zhang et al. demonstrated that the surface OVs in TiO_2 can induce a tail of the conduction band located above the H^+/H_2 redox potential, which extends its visible light adsorption [24]. Besides, OVs can promote the dissociation reaction of H_2O molecules to generate hydroxyl groups, which can be converted into hydroxyl radicals (·OH) by the holes to further oxidize refractory organic contaminants [25–28]. Moreover, the multi-dimensional structural TiO_2 with OVs can not only enhance the oxidative catalytic capability for degrading pollutants, but also effectively accelerates the photocatalytic HER [29,30]. However, a fast recombination rate of the photogenerated carriers still hinders the practical applications of the O-defect TiO_2. Considering the excellent electron transfer properties of MoS_2 with the active S-defect sites, a combination of TiO_2 with OVs and S-defect MoS_2 to form the dual-defect heterostructure can maximize the photogenerated carrier separation efficiency.

In this work, we design the dual-defect functional material for bifunctional purposes via a facile strategy, which combines the advantages of the unique S and O dual-defect structure in a MoS_2 @TiO_2 composite for solar-driven energy resource recovery and water treatment. We fabricated the 2D noble-metal-free ultrathin MoS_{2-x} nanosheets onto 3D TiO_2 hierarchical microspheres (TiO_2 HM) with delicate OVs via a hydrothermal method. X-ray photoelectron spectroscopy (XPS) and electron paramagnetic resonance (EPR) spectroscopy were used to demonstrate its dual-defect structure. Furthermore, density functional theory calculations and EPR analyses were employed to reveal the intrinsic mechanism of ·OH generation and the HER activity of this hybrid system. Upon treating the simulated pharmaceutical and coking wastewater, the catalyst presents the efficient hydrogen evolution performance and a high mineralization rate towards the organic pollutants. This work offers a new insight into the development of dual-defect materials for dual-functional photocatalysis, and further demonstrates the potential application of photocatalytic H_2 production integrated with oxidation of recalcitrant organic contaminants.

2. Experimental section

2.1. Chemicals

N, N-dimethylformamide (DMF, ≥99%), triethanolamine (TEOA, ≥99%), titanium isopropoxide (TIP, ≥97%), sodium molybdate dihydrate ($Na_2MoO_4.2\ H_2O$, ≥99%), thioacetamide (TAA, ≥99.0%), ofloxacin (OFX, ≥98%), enrofloxacin (ENR, ≥98%), ciprofloxacin (CIP, ≥98%), bisphenol A (BPA, ≥99%), phenol (≥99%), indole (≥99%),

pyridine (≥99%), and quinoline (≥99%) were purchased from Aladdin (Shanghai China). All reagents were at the analytical grade and used without further purification.

2.2. Synthesis of TiO2 HM and TiO2-OV

TiO_2 HM was synthesized via a facile solvothermal method. DMF (20 mL) was mixed with TEOA (40 mL) under vigorous stirring for 1 h to obtain a homogeneous transparent solution. Subsequently, TIP (2 mL) was added dropwise into the above mixture for another 30 min while stirring. The mixture was transferred into a Teflon-lined stainless-steel autoclave with a total volume of 100 mL. The hydrothermal synthesis was conducted at 200 °C for 24 h in an electric oven. The white precipitate was washed with deionized water and ethanol several times, and dried at 60 °C for 12 h. Samples were then calcinated in air at a ramp rate of 10 °C min^{-1} for 2 h and maintained at 500 °C for another 2 h in an electric muffle furnace. A prior method for synthesis of TiO_2-OV was used by chemical reduction with $NaBH_4$ [31,32]. 150 mg of as-synthesized TiO_2 HM powder sample and 75 mg of $NaBH_4$ were completely grounded by using a mortar for 15 min. The mixture was then transferred into a porcelain crucible sealed with tin foil and a cap, annealed to 350 °C at a heating rate of 10 °C min^{-1}, and maintained for 1 h. After cooling to room temperature in air, the obtained powder was washed with deionized water and ethanol several times to remove the unreacted $NaBH_4$, and then dried at 60 °C.

2.3. Synthesis of MoS2-x @ TiO2 and MoS2-x @ TiO2-OV

Defect-rich MoS_2 nanosheets were synthesized by following a previously reported hydrothermal method with a minor modification [33]. Firstly, TAA (60 mg) and $Na_2MoO_4.2\ H_2O$ (30 mg, the molar ratio of Mo: S = 1:6.5) were dissolved in deionized water (35 mL) to form a transparent solution. Next, TiO_2 HM (or TiO_2-OV, 80 mg) powder was added into the solution and stirred to form a homogeneous suspension. The mixture was then transferred to a Teflon-lined stainless-steel autoclave and heated in an electric oven at 200 °C for 24 h. The gray product (25% MoS_{2-x} @TiO_2 or 25% MoS_{2-x} @TiO_2-OV, % stands for weight percent) was harvested after thoroughly washing with deionized water and ethanol, and dried at 60 °C for 12 h. Similarly, by changing the mass ratio of the MoS_{2-x} precursors, MoS_{2-x} @TiO_2-OV with different MoS_{2-x} loading amounts (15%, 50%, and 75%) was obtained.

2.4. Photocatalytic hydrogen production

The photocatalytic water splitting reaction was carried out in a 250 mL photoreactor connected to a glass closed circulation system. A 300 W Xe lamp (CEL-HXF300, Ceaulight Co. Ltd. Beijing, China) was used as a simulated solar light source. Typically, the photocatalyst was dispersed in 100 mL of aqueous solution containing 20 mL of TEOA as the sacrificial reagent, the mixed solution was thoroughly degassed several times to remove the dissolved air, and then the amount of evolved H_2 was determined by on-line gas chromatography (CG1690, TCD, 5 Å molecular sieves column) using argon as the carrier gas. During the photocatalytic reaction, the temperature of the solution was kept below 293 K by a cooling water bath.

The apparent quantum yield (AQY) for H_2 evolution in the photocatalytic water splitting was measured under the illumination of a 300 W Xe lamp with different bandpass filters (λ = 400 ± 10, 420 ± 10, 425 ± 10, 450 ± 10, 500 ± 10, 550 ± 10 and 650 ± 10 nm) used to provide the monochromatic light. The number of incident photons was determined using a spectrometer (CEL-NP2000–2). Generally, the AQY value was calculated according to equation (1):

$$\text{AQY (\%)} = \frac{\text{Number of reacted electrons}}{\text{Number of incident photos}} \times 100\%$$
$$= \frac{\text{Number of evolved } H_2 \text{ molecules} \times 2}{\text{Number of incident photos}} \times 100\% \quad (1).$$

2.5. Photocatalytic pollutant degradation and simultaneous H₂ evolution

The photocatalytic activities of as-synthesized samples were evaluated by the degradation of typical refractory organic pollutants (OFX, ENR, CIP, and BPA) and the stimulated coking wastewater containing four common bio-recalcitrant contaminants (phenol, indole, pyridine, quinoline). A 300 W Xe lamp was used as a simulated solar light source. The solid catalyst was dispersed in a 100 mL solution containing organic pollutants. An aqueous solution was added into a Pyrex top-irradiation reaction vessel connected to a glass-closed gas system. The whole reaction setup was evacuated by a vacuum pump to completely remove air. High-purity argon gas was used as a carrier gas. Before irradiation, the solution was stirred in the dark for 1 h to reach an adsorption-desorption equilibrium, and the amount of hydrogen evolution from photocatalytic water splitting was analyzed using an online gas chromatograph. The temperature of the reaction solution was maintained at 293 K by an external flow of cold water.

2.6. Theoretical calculation

Density functional theory (DFT) calculations were performed in the Vienna ab initio simulation package (VASP). A spin-polarized GGA PBE functional, all-electron plane-wave basis set with an energy cutoff of 400 eV, and a projector augmented wave (PAW) method was adopted. A $(3 \times 3 \times 1)$ Monkhorst-Pack mesh was used for the Brillouin-zone integrations to be sampled. The conjugate gradient algorithm was used in the optimization. The convergence threshold was set at $1 * 10^{-4}$ eV in total energy and 0.05 eV/Å in force on each atom. The simulated surface structure of different samples is shown in Fig. S1.

The adsorption energy change (ΔE_{abs}) was determined as follows:

$$\Delta E_{abs} = E_{total} - E_{sur} - E_{H2O/H}$$

where E_{total} is the total energy for the adsorption state, E_{sur} is the energy of the pure surface, $E_{H2O/H}$ is the energy of H₂O or H.

The free energy change (ΔG) for adsorption was determined as follows: [34].

$$\Delta G = E_{total} - E_{sur} + \Delta E_{ZPE} - T\Delta S$$

where E_{total} is the total energy for the adsorption state, E_{sur} is the energy of the pure surface, ΔE_{ZPE} is the zero-point energy change and ΔS is the entropy change. As the vibrational entropy of H* in the adsorbed state is small, the entropy of adsorption of 1/2 H₂ is $S_H \approx -0.5S_0H_2$, where S_0H_2 is the entropy of H₂ in the gas phase under standard conditions. Therefore, the overall corrections were taken as in.

$$\Delta G_{H^*} = E_{total} - E_{sur} - E_{H2}/2 + 0.24 \text{ eV}$$

where E_{H2} is the energy of H₂ in the gas phase.

3. Results and discussion

3.1. Catalyst synthesis and characterization

The 2D/3D MoS₂₋ₓ @TiO₂-OV was synthesized with TiO₂ hierarchical microspheres as the preparation scheme displayed in Fig. 1. The hierarchical structure and the constituent nanosheets of the 3D TiO₂ HM can be easily identified by the SEM image. The diameter of the TiO₂ HM ranged ~3–7 μm while the thickness of the self-assembled nanosheets was ~20 nm (Fig. S2a). The pure MoS₂₋ₓ nanosheets were obtained via the same hydrothermal method by reacting sodium molybdate dihydrate with thioacetamide in the absence of TiO₂ HM. These self-assembled into a vesicular-like structure with the width ranging from 100 to 200 nm (Fig. S2b). SEM images of MoS₂₋ₓ @TiO₂-OV heterostructures (with 25% of MoS₂₋ₓ, see the experimental section for details) are shown in Fig. 2a and S2 c-d. Clearly, the 2D MoS₂₋ₓ nanosheets were uniformly and tightly coated on the top of 3D TiO₂ HM. In parallel, the
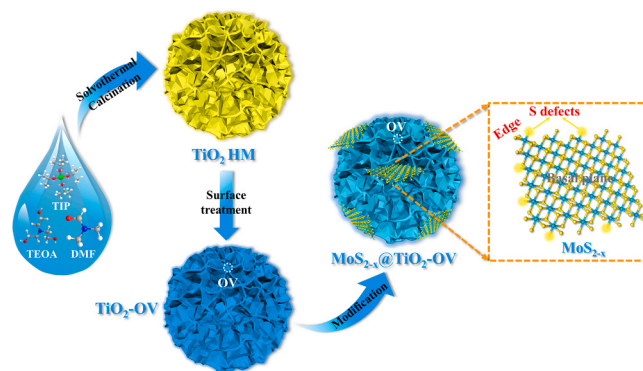

Fig. 1. Schematic illustration of the synthesis procedure of MoS₂₋ₓ @TiO₂-OV.

SEM-EDS mapping showed that Mo, S, Ti, and O elements were uniformly distributed. The EDS results showed the absence of Na and B elements, suggesting that the by-products from NaBH₄ can be easily removed by washing with water and ethanol (Fig. S3 and S4). With a higher magnification, we observe the gauze-like morphology of MoS₂₋ₓ nanosheets, intimately wrapped on the surface of self-assembled TiO₂ and fully integrated with TiO₂ HM (Fig. S2d and inset). It suggested that the intrinsic 3D TiO₂ hierarchical structure can prevent the 2D MoS₂₋ₓ nanosheets from restacking, thereby keeping its few-layer nanosheet structure. Evidently, the multi-level and multi-dimensional structures of the MoS₂₋ₓ @TiO₂-OV composite has been successfully constructed. This result will be supported by TEM characterization as further discussed below.

Fig. S5a displays the typical TEM image of a MoS₂₋ₓ @TiO₂-OV sample. Firstly, TEM observation correlated with SEM results; it showed the same hierarchical microspheres structure of TiO₂ and few layer nanosheets structure of MoS₂₋ₓ. Moreover, no scattered nanosheets can be observed in the TEM images, suggesting the tight interaction between MoS₂₋ₓ and TiO₂-OV. An apparent heterointerface boundary between MoS₂₋ₓ and TiO₂-OV can be found in the HR-TEM image (Fig. 2b). TiO₂-OV showed the visible lattice fringes with an interplanar distance of 0.343 nm, which matched well with the (101) plane of tetragonal TiO₂. The SAED pattern (Fig. S5b) also showed the tetragonal crystalline pattern characteristic of the anatase TiO₂ HM [35]. As shown in Fig. 2b-c, the ultrathin few layers MoS₂₋ₓ nanosheets were mostly distributed at the edges of nanosheets of TiO₂ microspheres. Fig. 2c shows the interplanar spacing of 0.620 nm of MoS₂₋ₓ consistent with the d spacing of the (002) planes of the hexagonal MoS₂₋ₓ crystal [36]. Many dislocations and distortions are observed in MoS₂₋ₓ nanosheets throughout the edges and cross-section (as marked by the white dashed circles in Fig. 2c and inset), which suggested a novel defect-rich structure [20,37]. Furthermore, the HAADF-STEM and corresponding EDS mapping images (Fig. 2d-g and S5c-d) demonstrated the homogeneous distribution of Ti, O, Mo, and S elements in the whole composite. All the above results demonstrate that the 2D MoS₂₋ₓ ultrathin nanosheets have been successfully incorporated into 3D TiO₂ HM.

According to the XRD pattern, the hydrothermal reaction product was amorphous (Fig. S6a). After calcining, TiO₂ HM was composed of the pure anatase crystallites (JCPDS 21–1272). After the surface treatment with NaBH₄, the intensity of the typical (101) peak at 25° was enhanced. The typical (002) peak of the MoS₂₋ₓ nanosheets (Fig. S6b) was not found in the XRD pattern of the MoS₂₋ₓ @TiO₂ and MoS₂₋ₓ @TiO₂-OV composite, possibly due to the ultrathin nature of MoS₂₋ₓ. To further validate the exact composition of the hybrid structures, Raman spectra of the TiO₂ HM and MoS₂₋ₓ @TiO₂-OV are illustrated in Fig. 3a. The pure TiO₂ HM sample had four peaks appearing at 144, 395, 514, and 640 cm⁻¹, which can be assigned to the E₁g, B₁g, A₁g+B₁g, and Eg vibration modes of the anatase TiO₂, respectively [38]. Besides, the E₁g, B₁g, and A₁g+B₁g peaks corresponded to the symmetric stretching
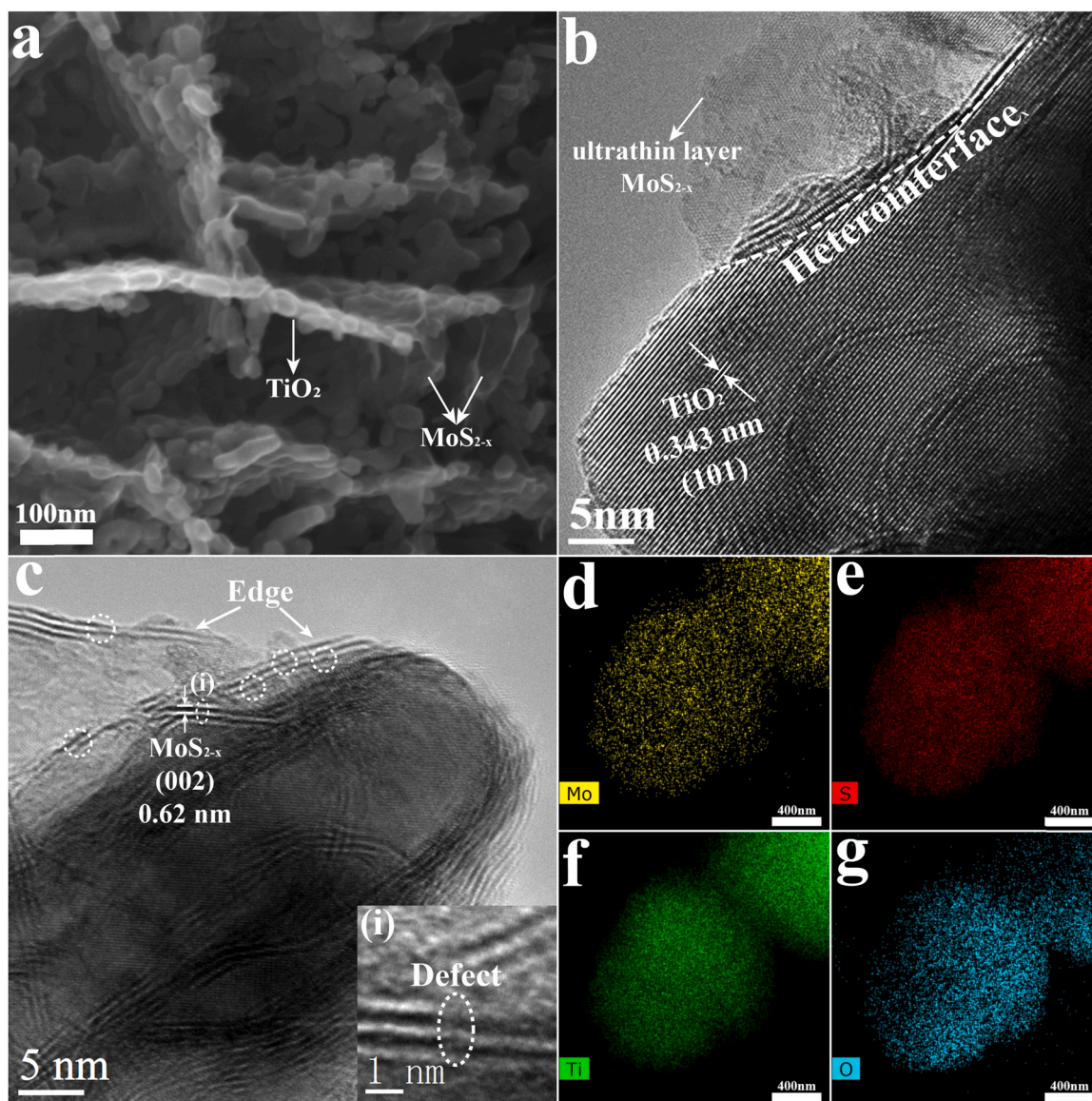
Fig. 2. (a) SEM and (b-c) HR-TEM images of 25% MoS_{2-x} @TiO_2-OV, inset is the HR-TEM image of selective area. (d-g) EDS mapping images show the homogeneous distribution of Mo (yellow), S (red), Ti (green), and O (blue). (For interpretation of the references to colour in this figure legend, the reader is referred to the web version of this article.)

vibration, symmetric bending vibration, and antisymmetric bending vibration of O-Ti-O, respectively. Compared to the TiO_2 HM, the main peak of MoS_{2-x} @TiO_2-OV at 150 cm^{-1} showed a distinct blue-shift and broadening of the Eg peak after $NaBH_4$ reduction, which might be caused by the formation of defects [31,39]. Moreover, the two dominant Raman scattering peaks emerged at 385 and 403 cm^{-1} in the MoS_{2-x} @TiO_2-OV sample corresponding to the E_{2g1} and A_{1g} modes of the MoS_{2-x} (Fig. S6c). Moreover, in the ATR-FTIR spectra of MoS_{2-x} @TiO_2-OV (Fig. 3b), the peak at 1120 cm^{-1} was assigned to the S-O asymmetric stretching. The successful identification of the covalent S-O bonds clarified that the MoS_{2-x} nanosheets are chemically anchored onto TiO_2 HM.

3.2. Identification of the dual-defect heterostructures

To verify the existence of the dual-defect structure in the composite, XPS and EPR measurements were conducted. The full XPS survey spectrum indicated the presence of Ti, O, Mo, and S elements in MoS_{2-x} @TiO_2-OV composite (Fig. S7). As shown in Fig. 3c, the O1s band can be

deconvoluted into two peaks corresponding to the lattice O and surface OVs, demonstrating the successful construction of OVs onto the surface of TiO_2 HM. These results agree well with the previous report [39]. Furthermore, EPR spectra were employed to confirm the dual-defect structure in the composite. According to Fig. 3d, TiO_2-OV showed an enhanced peak intensity compared to TiO_2 HM, suggesting the successful introduction of OVs. Unexpectedly, MoS_{2-x} @TiO_2 exhibited a sharp EPR signal with g = 2.004, which is attributed to the presence of unsaturated S sites in MoS_{2-x} nanosheets [40]. The EPR signal intensity of MoS_{2-x} @TiO_2-OV was lower than that of MoS_{2-x} @TiO_2, owing to the partial repair of S defects by the TiO_2-OV [41,42]. Additionally, compared to TiO_2 HM (59.96 $m^2\,g^{-1}$), the decrease in the specific surface area of MoS_{2-x} @TiO_2-OV (53.27 $m^2\,g^{-1}$) can also indirectly reflect the decrease of the defect densities (Fig. S8). Combined with the XPS results, it can be concluded that the dual-defect structure, which might improve the photocatalyst's optical adsorption and electronic properties, was successfully constructed in the MoS_{2-x} @TiO_2-OV composite.

The optical properties of the photocatalysts were investigated by UV–vis absorption spectroscopy. As shown in Fig. S9a, TiO_2 HM
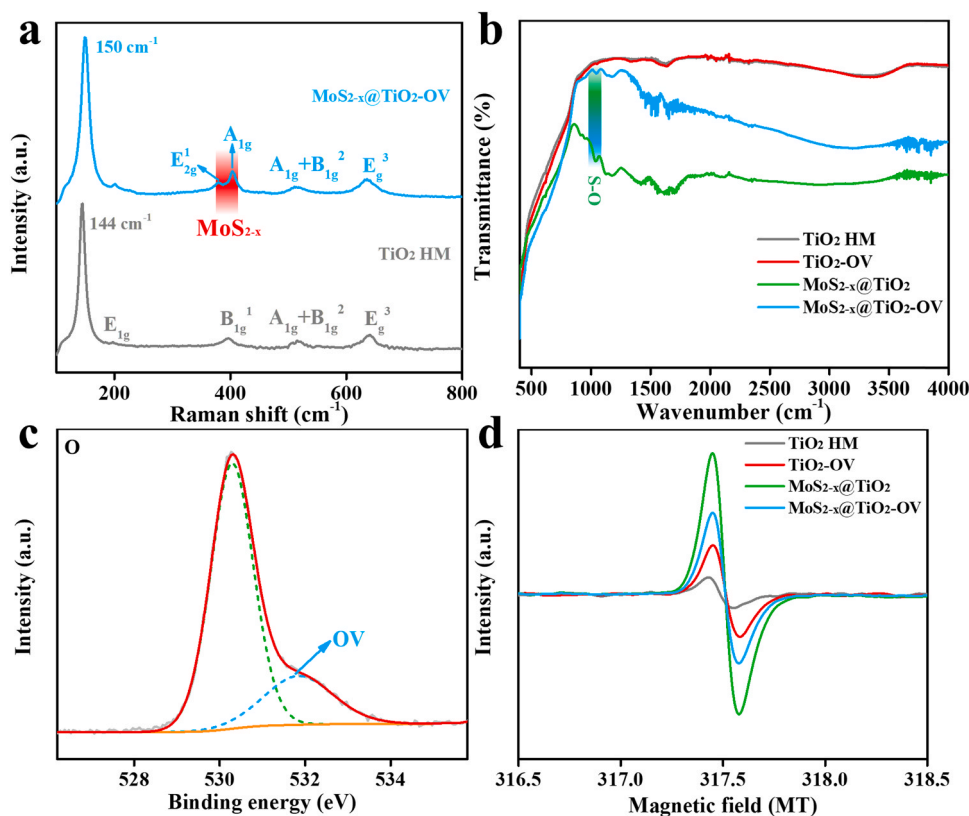
Fig. 3. (a) Raman spectra of TiO_2 HM and 25% MoS_{2-x} @TiO_2-OV, (b) ATR-FTIR spectroscopy of TiO_2 HM, TiO_2-OV, 25% MoS_{2-x} @TiO_2, and 25% MoS_{2-x} @TiO_2-OV, (c) High-resolution O 1 s XPS spectrum of 25% MoS_{2-x} @TiO_2-OV, (d) EPR spectroscopy of TiO_2 HM, TiO_2-OV, 25% MoS_{2-x} @TiO_2, and 25% MoS_{2-x} @TiO_2-OV.

exhibited a sharp absorption band edge at 418 nm. After $NaBH_4$ treatment, TiO_2-OV displayed an addition of a relatively broad adsorption in the visible light region, which together with the main absorption band edge extended to 426 nm. Compared to the pure TiO_2 HM, the absorption spectra of MoS_{2-x}, MoS_{2-x} @TiO_2, and MoS_{2-x} @TiO_2-OV showed a broadened absorption in the visible light region ranging from 400 to 800 nm. The corresponding energy bandgaps (Eg) are shown in Fig. S9b-c. Compared to the Eg value of the pristine TiO_2 HM (2.96 eV), the Eg value of TiO_2-OV was reduced to 2.91 eV. The corresponding flat band potential was reduced by 0.05 eV, which is attributed to the introduction of defects. The conduction band (CB) potentials of TiO_2 HM, TiO_2-OV, and MoS_{2-x} were − 0.32, − 0.27, and − 0.22 eV, respectively, according to Mott-Schottky plots (Fig. S9d-f). Subtracting from the CB, the valence band (VB) potentials of TiO_2 HM, TiO_2-OV, and MoS_{2-x} were determined to be 2.64, 2.66, and 1.06 eV, respectively. The above result demonstrates that OVs altered the band structure and enhanced the surface oxidation ability of TiO_2 HM. Furthermore, DFT calculations were performed to gain an insight into the band structure and the roles of the defect energy levels of O and S (Fig. S9g). The band gap of MoS_{2-x} @TiO_2-OV was theoretically calculated to be 0.05 eV. Besides, a density of states (DOS) calculation revealed that the generation of O and S defects caused localized electronic states composed of the Ti 3d and Mo 4d orbitals, respectively, to appear below the CB minimum. The band alignments of TiO_2-OV and MoS_{2-x} nanosheets are shown in Fig. S9h. Since the CB position of MoS_{2-x} matches that of TiO_2-OV, under light excitation condition, the photogenerated electrons in the VB can be excited and captured by the shallow OV energy level below the CB, and further transmitted to MoS_2 and accumulated by the sulfur-defect energy level [43–45]. The band structure of the dual-defect MoS_{2-x} @TiO_2-OV composite is beneficial for the charge transfer from TiO_2-OV to MoS_{2-x} and the subsequent photocatalytic hydrogen production.

3.3. Photogenerated carrier properties

To investigate the separation and transmission efficiency of photogenerated carriers, the steady-state PL spectra are displayed in Fig. S10. As the emission intensity originates from their recombination, the main characteristic shoulder emission peaks at 648 and 671 nm can be observed in the pristine TiO_2 HM upon excitation by the light with a wavelength of 325 nm, leading to robust recombination between the photogenerated electron-hole pairs [20,46]. Compared to TiO_2 HM, TiO_2-OV exhibited a slightly weaker PL intensity, indicating that the limitation of OVs is speeding up the charge separation process in a single-defect system. With the modification of MoS_{2-x} nanosheets, the PL emission was remarkably quenched by the introduction of the unsaturated S defect sites. The PL emission intensity was further decreased in the case of MoS_{2-x} @TiO_2-OV. Furthermore, the nanosecond time-resolved emission showed a faster decay of MoS_{2-x} @TiO_2-OV than that of the pristine TiO_2 HM. The average lifetimes of the emission decay for TiO_2 HM, TiO_2-OV, MoS_{2-x} @TiO_2, and MoS_{2-x} @TiO_2-OV were 0.434, 0.386, 0.375, and 0.320 ns (Fig. 4a). The gradually reduced lifetime from the above samples demonstrates that charge separation processes in MoS_{2-x} @TiO_2-OV were much more efficient than those in TiO_2-OV and MoS_{2-x} @TiO_2 [45]. The aforementioned phenomenon is attributed to the synergistic presence of O and S defects to effectively separate the photo-excited electron-hole pairs. The electron transfer ability on the composite interface was further evaluated by EIS. As shown in Fig. 4b, the Nyquist plots of MoS_{2-x} @TiO_2-OV samples had a smaller arc radius than those of TiO_2 HM, TiO_2-OV, and MoS_{2-x} @TiO_2, suggesting a remarkable decrease in the charge transfer resistance. The result revealed that an appropriate concentration of defects can greatly enhance the intrinsic conductivity of the composite, thus increasing the charge transfer efficiency and overall reaction efficiency. Besides, the three-dimensional charge density differences have been employed to
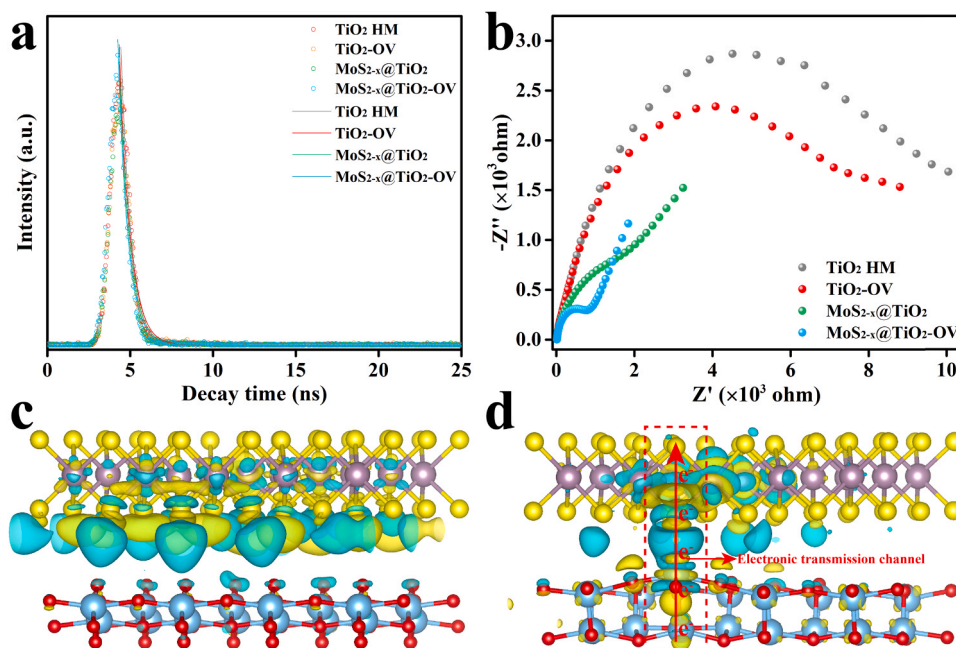
Fig. 4. (a) Time-resolved PL spectra, (b) EIS plots of TiO₂ HM, TiO₂-OV, 25% MoS₂₋ₓ @TiO₂, and 25% MoS₂₋ₓ @TiO₂-OV samples. The charge density difference distribution between MoS₂₋ₓ nanosheets and (c) TiO₂ HM or (d) TiO₂-OV. The yellow and blue parts represent the charge accumulation and depletion in the space, respectively. (For interpretation of the references to colour in this figure legend, the reader is referred to the web version of this article.)

unveil the charge distribution modulated by defects in composites. The results are shown in Fig. 4c-d. Compared with the single-defect MoS₂₋ₓ @TiO₂, the charge was mainly distributed at the interface of the dual-defect MoS₂₋ₓ @TiO₂-OV heterostructure, indicating the substantial effective charge transfer through the presence of dual defects on both MoS₂ and TiO₂ [42–47]. Moreover, Fig. S11 shows the electronic

structure (valence band maximum (VBM) and conduction band minimum (CBM)) of MoS₂₋ₓ @TiO₂ and MoS₂₋ₓ @TiO₂-OV. The VBM and CBM states of MoS₂₋ₓ @TiO₂ are only dominated in the MoS₂₋ₓ layer, suggesting the photo-excited electrons cannot be effectively transferred from the conduction band of TiO₂ HM to MoS₂₋ₓ. After the introduction of OV to form the dual-defect structures, the charge is prone to
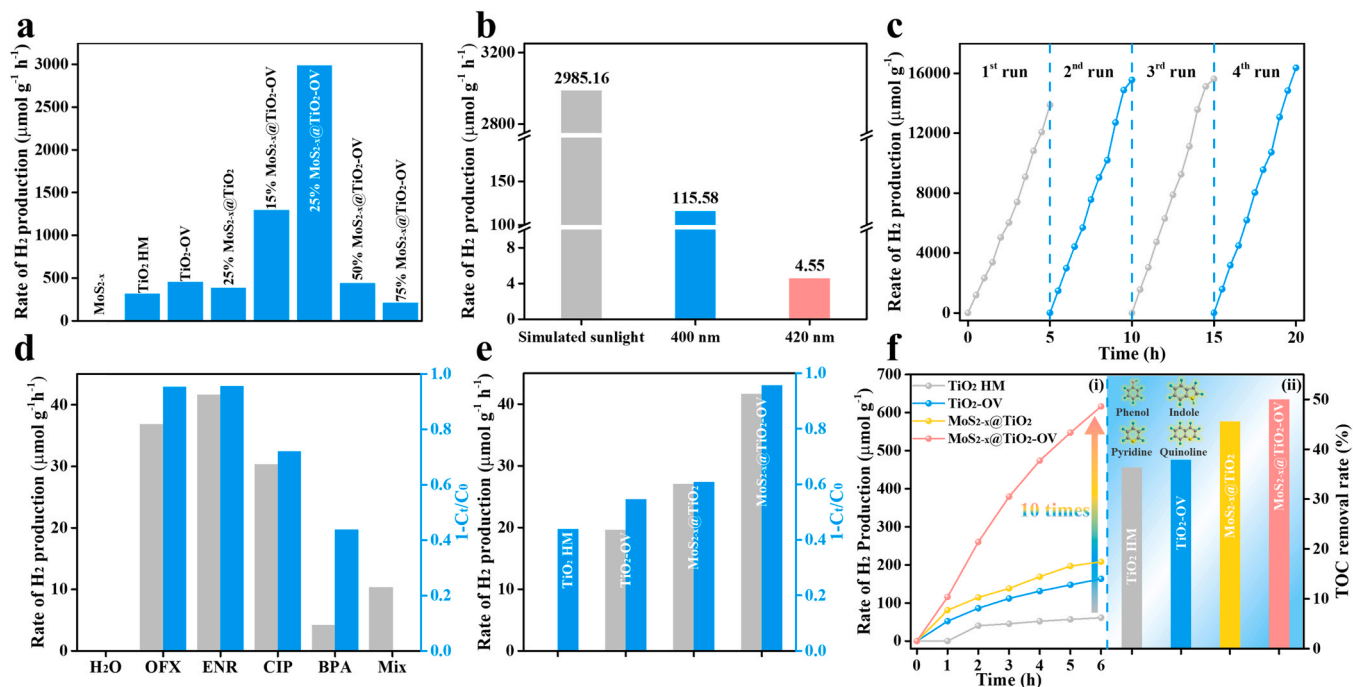

Fig. 5. (a) Rate of photocatalytic H₂ production of different catalysts in solution with TEOA under simulated solar light, (b) Rate of photocatalytic H₂ evolution performance of 25% MoS₂₋ₓ @TiO₂-OV with different wavelength cutoff filters (λ = 400 or 420 nm), (c) Stability test of H₂ evolution for 25% MoS₂₋ₓ @TiO₂-OV, (d) Simultaneous photocatalytic H₂ evolution and the degradation efficiency of different pollutants over 25% MoS₂₋ₓ @TiO₂-OV after 3 h. (e) Rate of photocatalytic H₂ production and the degradation efficiency of different catalysts in solution with ENR as electron donors. (f) Simultaneous photocatalytic H₂ evolution and mineralization rate of the simulated coking wastewater containing four common pollutants (phenol, indole, pyridine, quinoline). Conditions: catalysts dose = 0.15 g L⁻¹, initial concentration = 20 mg L⁻¹.

accumulate between Ti and S [48,49]. It also forms a convenient electron transfer channel between the TiO$_2$-OV and MoS$_{2-x}$ heterostructure under light excitation, which is favorable for charge separation. It indicates that the dual-defect MoS$_{2-x}$@TiO$_2$-OV heterostructure would be beneficial for HER.

3.4. Photocatalytic water splitting

The H$_2$ evolution reaction was subsequently carried out to evaluate the catalytic performance of photocatalysts without noble metal co-catalysts by using TEOA as sacrificial reagent under simulated solar light or visible light irradiation. As shown in Fig. 5a, the pure MoS$_{2-x}$ nanosheets showed a negligible PHE activity. TiO$_2$ HM exhibited a modest photocatalytic activity (315.2 µmol g^{-1}h^{-1}). Benefiting from the abundant OVs structures, TiO$_2$-OV possessed a dramatically improved H$_2$ evolution rate (452.6 µmol g^{-1}h^{-1}). Incorporating TiO$_2$-OV with 25% MoS$_{2-x}$ (MoS$_{2-x}$@TiO$_2$-OV) exhibited the highest PHE activity with an H$_2$ evolution of 2985.16 µmol g^{-1}h^{-1}, which was 6.59 and 7.78 times higher than TiO$_2$-OV and 25% MoS$_{2-x}$@TiO$_2$, respectively. Notably, it is worth mentioning that the photocatalytic hydrogen generation rate of 25% MoS$_{2-x}$@TiO$_2$-OV was 3.57 times than the sum of TiO$_2$-OV and 25% MoS$_{2-x}$@TiO$_2$. The superior PHE performances of 25% MoS$_{2-x}$@TiO$_2$-OV can be ascribed to the synergistic effects of the active OVs sites and dynamic unsaturated sulfur sites along the edges of the MoS$_{2-x}$ catalyst. In addition, the H$_2$ production rate of 25% MoS$_{2-x}$@TiO$_2$-OV was 115.58 under visible light irradiation ($\lambda > 400$ nm), indicating that the optimized photocatalyst had a good visible light response (Fig. 5b). Also, under the visible light irradiation ($\lambda > 420$ nm), the catalyst yields a hydrogen production rate at 4.55 µmol g^{-1}h^{-1}. As shown in Fig. S12, the wavelength at 350 nm produced the highest AQY of 9.55%. Meanwhile, the AQY of photocatalytic H$_2$ evolution reaction at different wavelengths (365, 380, 400, 420, and 475 nm) corresponds to 5.33%, 2.46%, 0.11%, 0.06%, and 0.02%, respectively. It is noticeable that the AQY profile is consistent with the optical absorption curve of MoS$_{2-x}$@TiO$_2$-OV, clearly indicating that the H$_2$ evolution activity of the photocatalyst strongly depends on the properties of light absorption and the active dual-defect sites. In addition to the conversion efficiency, the reusability and stability of the photoactivity of the catalysts is crucial for the practical applications (Fig. 5c). After each reaction cycle with a 5 h interval, the photocatalytic hydrogen production efficiency of the 25% MoS$_{2-x}$@TiO$_2$-OV composite presented a steadily increasing photocatalytic activity. The slightly increased activity might result from the in-situ activation of basal plane of MoS$_{2-x}$ in the photocatalytic conversion process, correlating well with a previous report [50]. The superior stability and durability of MoS$_{2-x}$@TiO$_2$-OV might be explained by the highly dispersed MoS$_2$ nanosheets onto the edges of TiO$_2$ HM, efficiently preventing the further aggregation of the catalyst. Furthermore, the MoS$_{2-x}$@TiO$_2$-OV composite was applied to PHE in pure water and natural seawater with TEOA as sacrificial agent, respectively. The results showed that the H$_2$ evolution performance of 25% MoS$_{2-x}$@TiO$_2$-OV in natural seawater is 1.49-fold better than in DI water (Fig. S13). It may be attributed that the alkali cations (e.g. Na$^+$, K$^+$) in seawater can coordinate with TEOA through electrostatic attraction and accelerate the separation of photogenerated carriers [51]. However, such photocatalytic hydrogen production process was achieved with the value-added sacrificial reagents.

3.5. Simultaneous photocatalytic water splitting and pollutant degradation

To explore the potential application of dual-functional composite materials in the hybrid field, simultaneous photocatalytic H$_2$ evolution and photodegradation of organic pollutants were investigated. Herein, we chose various common refractory organics pollutants, including enrofloxacin (ENR), ciprofloxacin (CIP), ofloxacin (OFX), bisphenol A (BPA), and bio-recalcitrant coking wastewater containing four typical

pollutants (phenol, pyridine, indole, quinoline) as the targeting water samples. As shown in Fig. 5d-e, the photocatalytic H$_2$ evolution rate was very low over MoS$_{2-x}$@TiO$_2$-OV in a solution containing BPA (4.12 µmol g^{-1}h^{-1}) solution. It can be concluded that the overlapping of electron clouds in the LUMO and HOMO of BPA will accelerate the recombination of photogenerated carriers, which is based on the computation of the frontier electron densities (Fig. S14 and Table S1) [52]. In addition, the degradation efficiency and mineralization rate of BPA reached 43.9% and 13.8%, respectively. It indirectly revealed that the electrons for the PHE reaction were originated from the oxidation of organic pollutants rather than water. In contrast, when ENR, OFX, or CIP was added in the photocatalytic system, the photocatalytic H$_2$ evolution rate can be markedly increased. The photocatalytic H$_2$ evolution rate followed the order of ENR (41.59 µmol g^{-1}h^{-1}) > OFX (36.82 µmol g^{-1}h^{-1}) > CIP (30.26 µmol g^{-1}h^{-1}). Accordingly, the degradation efficiency of ENR, OFX, and CIP was 95.6%, 95.3%, and 72.1%, respectively. The corresponding mineralization rates were determined to be 57.6%, 42.6%, and 24.3%, respectively (Fig. S15). The highest H$_2$ evolution rate of 41.59 µmol g^{-1}h^{-1} was achieved after degrading ENR. Meanwhile, the MoS$_{2-x}$@TiO$_2$-OV also exhibited excellent stability performance for simultaneous photocatalytic H$_2$ evolution and the high degradation efficiency (>95%) of ENR after four times of recycling (Fig. S16). The reason might be that the electron clouds of ENR are partially separated and possess a high HOMO orbital energy. The electrons extracted from degrading ENR could easily combine with the holes in TiO$_2$-OV, facilitating the photogenerated electrons to be transferred to the active S defect sites [52,53]. Moreover, MoS$_{2-x}$@TiO$_2$-OV can still achieve a 23.8% mineralization efficiency with a H$_2$ evolution rate of 10.31 µmol g^{-1}h^{-1} in a multi-pollutant wastewater system. Besides, the single-defect TiO$_2$-OV (19.55 µmol g^{-1}h^{-1}) and MoS$_{2-x}$@TiO$_2$ (41.59 µmol g^{-1}h^{-1}) samples also possessed a considerable photocatalytic H$_2$ evolution activity when using ENR to replace the traditional sacrificial agent (Fig. 5e). Moreover, as shown in Fig. S17, the MoS$_{2-x}$@TiO$_2$-OV catalyst exhibited simultaneous photocatalytic H$_2$ production and degradation efficiency in different water matrix including real wastewater, pearl river and DI water (the primary properties of water samples are shown in Table S2). Then the catalyst was further used to treat the simulated coking wastewater. As shown in Fig. 5 f, MoS$_{2-x}$@TiO$_2$-OV yields a H$_2$ production rate of 102.72 µmol g^{-1}h^{-1} which is 10.01, 3.77, and 2.96 times higher than TiO$_2$ HM, single-defect TiO$_2$-OV and MoS$_{2-x}$@TiO$_2$, respectively. And it presents a high mineralization rate of 50% towards the organic pollutants. It suggested that dual-defect structural MoS$_{2-x}$@TiO$_2$-OV is capability of recovering hydrogen energy and treating coking wastewater containing phenolic compounds and pharmaceutical wastewater. The overall dual-functional photocatalysis reactions were initiated by TiO$_2$ HM with OVs under simulated solar irradiation. First, OVs can drive the separation of photogenerated electron-holes under the influence of the built-in electric field [54,55]. Subsequently, the photogenerated holes at the surface/interface can further oxidize the hydroxyl groups to generate more·OH, which can then react with the pollutants in solution. At the same time, the photogenerated electrons at the CB of TiO$_2$-OV and electrons extracted from the decomposition of pollutants are transferred to the active S-defect sites of the MoS$_{2-x}$ nanosheets, facilitating the conversion of H$^+$ to produce H$_2$.

3.6. Mechanism of the simultaneous photocatalysis

To get a deeper understanding of the intrinsic mechanisms of the overall simultaneous photodegradation of pollutants and the H$_2$ evolution reaction, EPR spectroscopy and DFT calculations were carried out to explore the interaction between H$_2$O molecules and dual defects. First, to better comprehend the·OH generation pathway in the hybrid system, we have calculated the dissociation energy barrier of H$_2$O on MoS$_{2-x}$@TiO$_2$-OV. As shown in Fig. 6a, the theoretically calculated energy for the first step of O-H bond dissociation of H$_2$O molecules on TiO$_2$ HM,
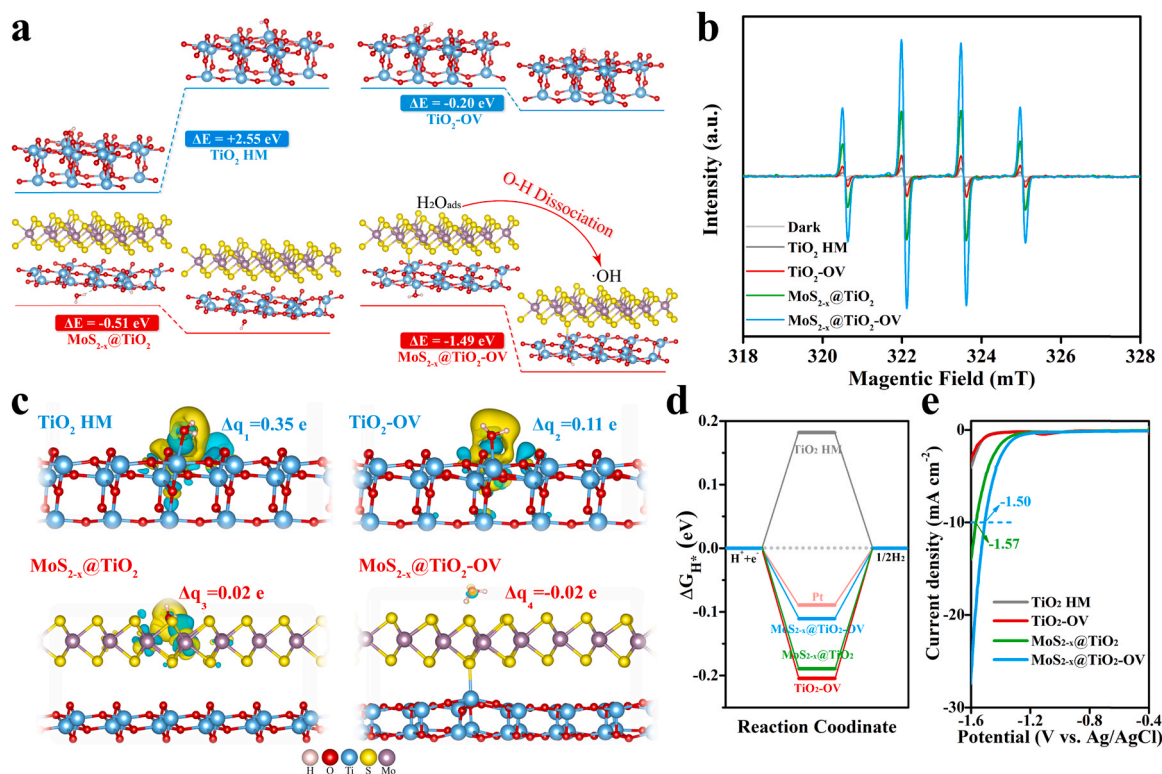
Fig. 6. (a) The dissociation energy barrier of single water to hydroxyl radicals on the different catalysts, (b) EPR spectra for the detection of·OH in the presence of 5,5-dimethyl-1-pyrrolidine N-oxide (DMPO), (c) Charge density difference distribution between catalysts and H_2O molecules, the yellow and blue parts represent the charge accumulation and depletion in the space, respectively. Δq is the Bader charge change of the adsorbed H_2O molecules. (d) The calculated Gibbs free energy diagram for H* adsorption (ΔG_{H*}) on the different catalysts and Pt reference, (e) LSV curves of TiO_2 HM, TiO_2-OV, 25% MoS_{2-x} @TiO_2, and 25% MoS_{2-x} @TiO_2-OV samples with a sweep rate of 10 mV s^{-1}, displaying the overpotential vs Ag/AgCl corresponding to the current density of 10 mA cm^{-2}. (For interpretation of the references to colour in this figure legend, the reader is referred to the web version of this article.)

TiO_2-OV, MoS_{2-x} @TiO_2, and MoS_{2-x} @TiO_2-OV was + 2.55, − 0.20, − 0.51, and − 1.49 eV, respectively. Obviously, the dissociation energy barrier of H_2O molecules on TiO_2-OV, MoS_{2-x} @TiO_2, and MoS_{2-x} @TiO_2-OV was more negative than that of pristine TiO_2 HM. It implied that the introduction of OVs and the loading of the MoS_{2-x} cocatalyst can efficiently promote the dissociation of H_2O molecules to·OH [56, 58]. Furthermore, the presence of·OH was determined by EPR spectroscopy using DMPO as the spin trapping agent under vacuum condition. As displayed in Fig. 6b, no peaks were observed when MoS_{2-x} @TiO_2-OV was not irradiated by light. In addition, MoS_{2-x} @TiO_2-OV, as expected, showed the strongest·OH characteristic signals relative to those of TiO_2 HM, TiO_2-OV, and MoS_{2-x} @TiO_2. It indicated that the dual-defect MoS_{2-x} @TiO_2-OV can significantly enhance the transformation of the surface hydroxyl groups to·OH via the photogenerated holes. The result of·OH generation performance correlated perfectly with theoretical results which indicate the trend of water dissociation and generation of·OH is as follows: TiO_2 HM < TiO_2-OV < MoS_{2-x} @TiO_2 < MoS_{2-x} @TiO_2-OV. It also directly verified the above-mentioned activity performance of synergistic treatment of coking wastewater containing phenolic compounds, which are easily attacked by hydroxyl radicals [55,59].

On the other hand, the differential charge density map was determined to analyze the Bader charge change between the adsorbed H_2O molecules and different catalysts (Fig. 6c). Herein, the calculated Bader charge is the sum of the Bader charges of two H atoms and one O atom. The negative change of the Bader charge indicates the transfer of electrons from the MoS_2 or TiO_2 surface to the adsorbed H_2O molecules [60]. In the HER process, electrons must transfer from the active sites of the catalyst to H_2O molecules. The Bader charge analysis revealed that H_2O two H atoms and one O atom. The negative change of the Bader charge indicates the transfer of electrons from the MoS_2 or TiO_2 surface

to the adsorbed H_2O molecules. In the HER process, electrons must transfer from the active sites of the catalyst to H_2O molecules. The Bader charge analysis revealed that H_2O molecules were adsorbed on the unsaturated S sites via a S-O-H bond and received 0.02e from MoS_{2-x} @TiO_2-OV. However, the direction of electron transfer for other catalysts is from H_2O to the catalyst, which is not beneficial to HER. In addition, the effect of coexistence of dual defects on the HER activity of MoS_{2-x} @TiO_2-OV was investigated by a DFT model calculation. Here, the Gibbs free energies for hydrogen adsorption (ΔG_{H*}) on the pristine TiO_2 HM and the composite are shown in Fig. 6d. The ΔG_{H*} is a key indicator of HER activity. If the H atom adsorption energy was positive, hydrogen generation would be difficult. Meanwhile, a smaller absolute value of ΔG_{H*} (close-to-zero) usually indicates a higher HER activity [61–63]. The calculated ΔG_{H*} value of the pristine TiO_2 HM was 0.230 eV. It meant that the TiO_2 HM surface had a weak affinity for adsorbing H* ; because the Volmer step was thermodynamically uphill, a relatively high overpotential is required to surpass it. On the contrary, the ΔG_{H*} value of TiO_2-OV was − 0.212 eV, indicating that the introduction of OVs was favorable for the adsorption of H* . Besides, the calculated ΔG_{H*} values of MoS_{2-x} @TiO_2 and MoS_{2-x} @TiO_2-OV were − 0.188 eV and − 0.112 eV. Here, it is worth mentioning that the calculated ΔG_{H*} of MoS_{2-x} @TiO_2-OV was much closer to the theoretical value of Pt ($\Delta G_{H*} = -0.090$ eV), a model HER catalyst. This implied that the dual-defect MoS_{2-x} @TiO_2-OV was much more effective than the single-defect MoS_{2-x} @TiO_2. Moreover, the LSV technique was performed to further characterize the HER performance of the catalysts. The result depicted in Fig. 6e shows that TiO_2 HM and TiO_2-OV displayed a negligible HER electrocatalytic activity, indicating that the TiO_2 HM substrate was not active for the HER. The polarization curves recorded with the MoS_{2-x} @TiO_2-OV (1.50 V vs Ag/AgCl) showed a lower overpotential at 10 mA cm^{-2} for the HER than MoS_{2-x} @TiO_2

(1.57 V vs Ag/AgCl). The lower overpotential indicated that protons were more easily reduced on the MoS_{2-x} @TiO_2-OV photocatalyst. On the one hand, with the assistance of OVs, MoS_{2-x} @TiO_2-OV displayed a more positive onset overpotential (η) and larger cathodic current density than MoS_{2-x} @TiO_2. It implied that the superior HER activity of MoS_{2-x} @TiO_2-OV was related to the synergic effect of OVs and more unsaturated sulfur sites along the edges. Moreover, it also indicated that the MoS_{2-x} nanosheets possessed the strong catalytic activity in converting H^+ to H_2. Therefore, combination of the ΔG_{H^*} calculation result with electron density analysis can well support the experimental results and unravel the mechanistic details of the superior performance of MoS_{2-x} @TiO_2-OV.

The excellent photocatalytic performance and good stability of MoS_{2-x} @TiO_2-OV in water splitting can be attributed to three aspects as follows: (i) the OVs can enhance the catalytic oxidation ability of the TiO_2 HM surface for efficient removal of pollutants; (ii) the 3D structure of TiO_2 HM with a large surface area can effectively reduce the agglomeration and stacking of 2D MoS_2 nanosheets; thus, ultrathin structures, which expose more active sulfur sites along with edges of MoS2can be formed; (iii) benefiting from the synergistic effect of the electron donor nature of rich OVs and the electron acceptor properties of S defects, this dual-defect structure can facilitate the initial photocarrier separation, charge transfer between the semiconductor-catalyst interface, and achieve an optimal affinity between H^+ and MoS_2. Therefore, the integrated optimization of the MoS_{2-x} @TiO_2-OV composite with the dual-defect structure are highly efficient towards photocatalytic energy recovery from pharmaceutical and coking wastewater treatment.

4. Conclusions

In summary, the dual-defect strategy and interface engineering were accomplished in the MoS_{2-x} @TiO_2-OV composite. This unique interface provides an unprecedented opportunity to synergistically modulate both the structure and distribution of defect sites for wastewater purification integrated with energy recovery. For the processes of dual-functional photocatalysis, the large area of 3D TiO_2 HM with abundant OVs can not only improve its catalytic oxidation ability for degrading pollutants, but also provide more active sites for dissociating H_2O molecules. The 2D MoS_{2-x} with an excess of unsaturated sulfur defects as electron acceptors can improve the interface's electron transfer efficiency towards producing H_2. The optimized MoS_{2-x} @TiO_2-OV composite exhibits a dramatically enhanced PHE activity with a rate as high as 2985.16 μmol $g^{-1}h^{-1}$, exceeding that of the single OV system (TiO_2-OV) and the sulfur-only-defect system (MoS_{2-x} @TiO_2) by 6.59 and 7.78-fold, respectively. Meanwhile, it also shows the remarkable synergistic effect in simultaneous photocatalytic H_2 evolution and wastewater treatment by using ENR as sacrificial agent. Upon treating the coking wastewater, the H_2 production rate of MoS_{2-x} @TiO_2-OV is superior to TiO_2 HM, single-defect TiO_2-OV and MoS_{2-x} @TiO_2. Exploiting the unique multi-dimensional structure and the novel TMD-based catalyst, it will offer new insights for tuning the interfacial charge transfer and utilization in the reaction processes of dual-functional photocatalysis. Furthermore, the simultaneous introduction of defects and interface engineering will provide a feasible strategy to enable dual-functional photocatalysts for potential multi-applications in environmental remediation and solar fuel production at the nexus of water and solar energy.

CRediT authorship contribution statement

Yaoyao Wu: Conceptualization, Data curation, Writing – original draft. **Xiaotao Chen:** Investigation, Data curation. **Jiachun Cao:** Methodology, Computational modeling. **Yuqing Zhu:** Investigation, Data curation. **Wenjing Yuan:** Investigation, Data curation. **Zhuofeng Hu:** Computational modeling. **Zhimin Ao:** Computational modeling and analysis. **Gary W. Brudvig:** Supervision, Resources, Writing – review & editing. **Fenghui Tian:** Methodology, Computational modeling. **Jimmy C. Yu:** Supervision, Writing – review & editing. **Chuanhao Li:** Supervision, Funding acquisition, Resources, Writing – review & editing.

Declaration of Competing Interest

The authors declare that they have no known competing financial interests or personal relationships that could have appeared to influence the work reported in this paper.

Acknowledgements

Appendix A. Supporting information

Supplementary data associated with this article can be found in the online version at doi:10.1016/j.apcatb.2021.120878.

References

[1] S. Kampouri, K.C. Stylianou, Dual-functional photocatalysis for simultaneous hydrogen production and oxidation of organic substances, ACS Catal. 9 (2019) 4247–4270, https://doi.org/10.1021/acscatal.9b00332.

[2] S. Kim, G. Piao, D.S. Han, H.K. Shon, H. Park, Solar desalination coupled with water remediation and molecular hydrogen production: a novel solar water-energy nexus, Energy Environ. Sci. 11 (2018) 344–353, https://doi.org/10.1039/C7EE02640D.

[3] D. Li, J.C.-C. Yu, V.-H. Nguyen, J.C.S. Wu, X. Wang, A dual-function photocatalytic system for simultaneous separating hydrogen from water splitting and photocatalytic degradation of phenol in a twin-reactor, Appl. Catal., B 239 (2018) 268–279, https://doi.org/10.1016/j.apcatb.2018.08.010.

[4] Y.-T. Lin, Y.-H. Wang, J.C.S. Wu, X. Wang, Photo-Fenton enhanced twin-reactor for simultaneously hydrogen separation and organic wastewater degradation, Appl. Catal., B 281 (2021), 119517, https://doi.org/10.1016/j.apcatb.2020.119517.

[5] J. Kim, D. Monllor-Satoca, W. Choi, Simultaneous production of hydrogen with the degradation of organic pollutants using TiO_2 photocatalyst modified with dual surface components, Energy Environ. Sci. 5 (2012) 7647–7656, https://doi.org/10.1039/C2EE21310A.

[6] T.H. Jeon, M.S. Koo, H. Kim, W. Choi, Dual-functional photocatalytic and photoelectrocatalytic systems for energy- and resource-recovering water treatment, ACS Catal. 8 (2018) 11542–11563, https://doi.org/10.1021/acscatal.8b03521.

[7] H. Belhadj, S. Hamid, P.K.J. Robertson, D.W. Bahnemann, Mechanisms of simultaneous hydrogen production and formaldehyde oxidation in H_2O and D_2O over Platinized TiO_2, ACS Catal. 7 (2017) 4753–4758, https://doi.org/10.1021/acscatal.7b01312.

[8] F. Deng, F. Zhong, D. Lin, L. Zhao, Y. Liu, J. Huang, X. Luo, S. Luo, D.D. Dionysiou, One-step hydrothermal fabrication of visible-light-responsive $AgInS_2$/$SnIn_4S_8$ heterojunction for highly-efficient photocatalytic treatment of organic pollutants and real pharmaceutical industry wastewater, Appl. Catal., B 219 (2017) 163–172, https://doi.org/10.1016/j.apcatb.2017.07.051.

[9] C. Dong, Z. Wang, Z. Ye, J. He, Z. Zheng, X. Gong, J. Zhang, I.M.C. Lo, Superoxide radicals dominated visible light driven peroxymonosulfate activation using molybdenum selenide ($MoSe_2$) for boosting catalytic degradation of pharmaceuticals and personal care products, Appl. Catal., B 296 (2021), 120223, https://doi.org/10.1016/j.apcatb.2021.120223.

[10] J. Hu, P. Zhang, W. An, L. Liu, Y. Liang, W. Cui, In-situ Fe-doped g-C_3N_4 heterogeneous catalyst via photocatalysis-Fenton reaction with enriched photocatalytic performance for removal of complex wastewater, Appl. Catal., B 245 (2019) 130–142, https://doi.org/10.1016/j.apcatb.2018.12.029.

[11] F.C. Moreira, R.A.R. Boaventura, E. Brillas, V.J.P. Vilar, Electrochemical advanced oxidation processes: a review on their application to synthetic and real wastewaters, Appl. Catal., B 202 (2017) 217–261, https://doi.org/10.1016/j.apcatb.2016.08.037.

[12] Y. Bai, Q. Sun, R. Sun, D. Wen, X. Tang, Bioaugmentation and adsorption treatment of coking wastewater containing pyridine and quinoline using zeolite-biological aerated filters, Environ. Sci. Technol. 45 (2011) 1940–1948, https://doi.org/10.1021/es103150v.

[13] P. Dalkmann, M. Broszat, C. Siebe, E. Willaschek, T. Sakinc, J. Huebner, W. Amelung, E. Grohmann, J. Siemens, Accumulation of pharmaceuticals, enterococcus, and resistance genes in soils irrigated with wastewater for zero to 100 years in central mexico, Plos One 7 (2012) https://doi.org/ARTN10.1371/journal.pone.0045397.

[14] L. Xue, J. Liu, M. Li, T. Liang, X. Ji, S. Shi, B. Jiang, Enhanced treatment of coking wastewater containing phenol, pyridine, and quinoline by integration of an E-Fenton process into biological treatment, Environ. Sci. Pollut. R. 24 (2017) 1–11, https://doi.org/10.1007/s11356-017-8644-y.

[15] Z. Hu, Z. Wu, C. Han, J. He, Z. Ni, W. Chen, Two-dimensional transition metal dichalcogenides: interface and defect engineering, Chem. Soc. Rev. 47 (2018) 3100–3128, https://doi.org/10.1039/C8CS00024G.

[16] Z. Wang, B. Mi, Environmental Applications of 2D Molybdenum Disulfide (MoS_2) Nanosheets, Environ. Sci. Technol. 51 (2017) 8229–8244, https://doi.org/10.1021/acs.est.7b01466.

[17] J. Kibsgaard, Z. Chen, B.N. Reinecke, T. Jaramillo, Engineering the surface structure of MoS_2 to preferentially expose active edge sites for electrocatalysis, Nat. Mater. 11 (2012) 963–969, https://doi.org/10.1038/NMAT3439.

[18] Q. Tang, D.-e Jiang, Mechanism of hydrogen evolution reaction on 1t-mos2 from first principles, ACS Catal. 6 (2016) 4953–4961, https://doi.org/10.1021/acscatal.6b01211.

[19] J. Xie, J. Zhang, S. Li, F. Grote, X. Zhang, H. Zhang, R. Wang, Y. Lei, B. Pan, Y. Xie, Controllable disorder engineering in oxygen-incorporated MoS_2 ultrathin nanosheets for efficient hydrogen evolution, J. Am. Chem. Soc. 135 (2013) 17881–17888, https://doi.org/10.1021/ja408329q.

[20] S. Kumar, A. Kumar, V. Navakoteswara Rao, A. Kumar, M.V. Shankar, V. Krishnan, Defect-rich MoS_2 ultrathin nanosheets-coated nitrogen-doped zno nanorod heterostructures: an insight into in-situ-generated zns for enhanced photocatalytic hydrogen evolution, ACS Appl. Energy Mater. 2 (2019) 5622–5634, https://doi.org/10.1021/acsaem.9b00790.

[21] A. Naldoni, M. Altomare, G. Zoppellaro, N. Liu, S. Kment, R. Zboril, P. Schmuki, Photocatalysis with reduced TiO_2: from black TiO_2 to cocatalyst-free hydrogen production, ACS Catal. 9 (2019) 345–364, https://doi.org/10.1021/acscatal.8b04068.

[22] M.K. Nowotny, L.R. Sheppard, T. Bak, J. Nowotny, Defect chemistry of titanium dioxide. application of defect engineering in processing of tio2-based photocatalysts, J. Phys. Chem. C 112 (2008) 5275–5300, https://doi.org/10.1021/jp077275m.

[23] X. Pan, M.-Q. Yang, X. Fu, N. Zhang, Y.-J. Xu, Defective TiO_2 with oxygen vacancies: synthesis, properties and photocatalytic applications, Nanoscale 5 (2013) 3601–3614, https://doi.org/10.1039/C3NR00476G.

[24] H. Zhang, J. Cai, Y. Wang, M. Wu, M. Meng, Y. Tian, X. Li, J. Zhang, L. Zheng, Z. Jiang, J. Gong, Insights into the effects of surface/bulk defects on photocatalytic hydrogen evolution over TiO_2 with exposed {001} facets, Appl. Catal., B 220 (2018) 126–136, https://doi.org/10.1016/j.apcatb.2017.08.046.

[25] Y. Nosaka, A. Nosaka, Understanding hydroxyl radical (●OH) generation processes in photocatalysis, ACS Energy Lett. 1 (2016) 356–359, https://doi.org/10.1021/acsenergylett.6b00174.

[26] W. Kim, T. Tachikawa, G.-h Moon, T. Majima, W. Choi, Molecular-level understanding of the photocatalytic activity difference between anatase and rutile nanoparticles, Angew. Chem., Int. Ed. 53 (2014) 14036–14041, https://doi.org/10.1002/anie.201406625.

[27] Y. Nosaka, A.Y. Nosaka, Generation and detection of reactive oxygen species in photocatalysis, Chem. Rev. 117 (2017) 11302–11336, https://doi.org/10.1021/acs.chemrev.7b00161.

[28] O. Bikondoa, C.L. Pang, R. Ithnin, C.A. Muryn, H. Onishi, G. Thornton, Direct visualization of defect-mediated dissociation of water on TiO_2(110), Nat. Mater. 5 (2006) 189–192, https://doi.org/10.1038/nmat1592.

[29] R. Shen, C. Jiang, Q. Xiang, J. Xie, X. Li, Surface and interface engineering of hierarchical photocatalysts, Appl. Surf. Sci. 471 (2019) 43–87, https://doi.org/10.1016/j.apsusc.2018.11.205.

[30] W. Zhang, Y. Tian, H. He, L. Xu, W. Li, D. Zhao, Recent advances in the synthesis of hierarchically mesoporous TiO_2 materials for energy and environmental applications, Natl. Sci. Rev. 7 (2020) 1702–1725, https://doi.org/10.1093/nsr/nwaa021.

[31] H. Shang, M. Li, H. Li, S. Huang, C. Mao, Z. Ai, L. Zhang, Oxygen vacancies promoted the selective photocatalytic removal of no with blue tio2 via simultaneous molecular oxygen activation and photogenerated hole annihilation, Environ. Sci. Technol. 53 (2019) 6444–6453, https://doi.org/10.1021/acs.est.8b07322.

[32] H. Tan, Z. Zhao, M. Niu, C. Mao, D. Cao, D. Cheng, P. Feng, Z. Sun, A facile and versatile method for preparation of colored TiO_2 with enhanced solar-driven photocatalytic activity, Nanoscale 6 (2014) 10216–10223, https://doi.org/10.1039/C4NR02677B.

[33] J. Xie, H. Zhang, S. Li, R. Wang, X. Sun, M. Zhou, J. Zhou, X.W. Lou, Y. Xie, Defect-rich MoS_2 ultrathin nanosheets with additional active edge sites for enhanced electrocatalytic hydrogen evolution, Adv. Mater. 25 (2013) 5807–5813, https://doi.org/10.1002/adma.201302685.

[34] J.K. Nørskov, T. Bligaard, A. Logadottir, J.R. Kitchin, J.G. Chen, S. Pandelov, U. Stimming, Trends in the exchange current for hydrogen evolution, J. Electrochem. Soc. 152 (2005) J23, https://doi.org/10.1149/1.1856988.

[35] B. Tan, X. Ye, Y. Li, X. Ma, Y. Wang, J. Ye, Defective Anatase $TiO_{2−x}$ Mesocrystal Growth In Situ on g-C_3N_4 Nanosheets: Construction of 3D/2D Z-Scheme Heterostructures for Highly Efficient Visible-Light Photocatalysis, Chem. -Eur. J. 24 (2018) 13311–13321, https://doi.org/10.1002/chem.201802366.

[36] Y.-J. Yuan, Z.-J. Ye, H.-W. Lu, B. Hu, Y.-H. Li, D.-Q. Chen, J.-S. Zhong, Z.-T. Yu, Z.-G. Zou, Constructing Anatase TiO_2 Nanosheets with Exposed (001) Facets/Layered MoS_2 Two-Dimensional Nanojunctions for Enhanced Solar Hydrogen Generation, ACS Catal. 6 (2016) 532–541, https://doi.org/10.1021/acscatal.5b02036.

[37] P. Basu, J. Chakraborty, N. Ganguli, K. Mukherjee, K. Acharya, B. Satpati, S. Khamrui, S. Mandal, D. Banerjee, D. Goswami, P.M.G. Nambissan, K. Chatterjee, Defect-engineered mos2 nanostructures for reactive oxygen species generation in the dark: antipollutant and antifungal performances, ACS Appl. Mater. Interfaces 11 (2019) 48179–48191, https://doi.org/10.1021/acsami.9b12988.

[38] L. Zheng, S. Han, H. Liu, P. Yu, X. Fang, Hierarchical MoS_2 nanosheet@tio2 nanotube array composites with enhanced photocatalytic and photocurrent performances, Small 12 (2016) 1527–1536, https://doi.org/10.1002/smll.201503441.

[39] W. Zhang, H. He, Y. Tian, H. Li, K. Lan, L. Zu, Y. Xia, L. Duan, W. Li, D. Zhao, Defect-engineering of mesoporous TiO_2 microspheres with phase junctions for efficient visible-light driven fuel production, Nano Energy 66 (2019), 104113, https://doi.org/10.1016/j.nanoen.2019.104113.

[40] L. Guo, C. Zhong, L. Shi, L. Ju, X. Wang, D. Yang, K. Bi, Y. Hao, Y. Yang, Phase and defect engineering of MoS_2 stabilized in periodic TiO_2 nanoporous film for enhanced solar water splitting, Adv. Opt. Mater. 7 (2019) 1801403, https://doi.org/10.1002/adom.201801403.

[41] H. Gao, R. Cao, X. Xu, S. Zhang, H. Yongshun, H. Yang, X. Deng, J. Li, Construction of dual defect mediated Z-scheme photocatalysts for enhanced photocatalytic hydrogen evolution, Appl. Catal., B 245 (2019) 399–409, https://doi.org/10.1016/j.apcatb.2019.01.004.

[42] S. Zhang, X. Liu, C. Liu, S. Luo, L. Wang, T. Cai, Y. Zeng, J. Yuan, W. Dong, Y. Pei, Y. Liu, MoS_2 Quantum Dot Growth Induced by S Vacancies in a $ZnIn_2S_4$ Monolayer: Atomic-Level Heterostructure for Photocatalytic Hydrogen Production, ACS Nano 12 (2018) 751–758, https://doi.org/10.1021/acsnano.7b07974.

[43] M. Xu, Y. Chen, J. Qin, Y. Feng, W. Li, W. Chen, J. Zhu, H. Li, Z. Bian, Unveiling the role of defects on oxygen activation and photodegradation of organic pollutants, Environ. Sci. Technol. 52 (2018) 13879–13886, https://doi.org/10.1021/acs.est.8b03558.

[44] J. Xiong, Y. Liu, D. Wang, S. Liang, W. Wu, L. Wu, An efficient cocatalyst of defect-decorated MoS_2 ultrathin nanoplates for the promotion of photocatalytic hydrogen evolution over CdS nanocrystal, J. Mater. Chem. A 3 (2015) 12631–12635, https://doi.org/10.1039/C5TA02438B.

[45] W. Wang, S. Zhu, Y. Cao, Y. Tao, X. Li, D. Pan, D.L. Phillips, D. Zhang, M. Chen, G. Li, H. Li, Edge-enriched ultrathin MoS_2 embedded yolk-shell TiO_2 with boosted charge transfer for superior photocatalytic H_2 evolution, Adv. Funct. Mater. 29 (2019) 1901958, https://doi.org/10.1002/adfm.201901958.

[46] N. Luo, C. Chen, D. Yang, W. Hu, F. Dong, S defect-rich ultrathin 2D MoS_2: the role of S point-defects and S stripping-defects in the removal of Cr(VI) via synergistic adsorption and photocatalysis, Appl. Catal., B 299 (2021), 120664, https://doi.org/10.1016/j.apcatb.2021.120664.

[47] X. Wang, Y. Zhang, H. Si, Q. Zhang, J. Wu, L. Gao, X. Wei, Y. Sun, Q. Liao, Z. Zhang, K. Ammarah, L. Gu, Z. Kang, Y. Zhang, Single-atom vacancy defect to trigger high-efficiency hydrogen evolution of MoS_2, J. Am. Chem. Soc. 142 (2020) 4298–4308, https://doi.org/10.1021/jacs.9b12113.

[48] W. Li, R. Long, J. Tang, O.V. Prezhdo, Influence of defects on excited-state dynamics in lead halide perovskites: time-domain ab initio studies, J. Phys. Chem. Lett. 10 (2019) 3788–3804, https://doi.org/10.1021/acs.jpclett.9b00641.

[49] W. Hu, L. Lin, R. Zhang, C. Yang, J. Yang, Highly efficient photocatalytic water splitting over edge-modified phosphorene nanoribbons, J. Am. Chem. Soc. 139 (2017) 15429–15436, https://doi.org/10.1021/jacs.7b08474.

[50] W. Xun, Y. Wang, R. Fan, Q. Mu, S. Ju, Y. Peng, M. Shen, Activating the MoS_2 basal plane toward enhanced solar hydrogen generation via in situ photoelectrochemical control, ACS Energy Lett. 6 (2021) 267–276, https://doi.org/10.1021/acsenergylett.0c02320.

[51] W. Xu, X. Zhao, X. An, S. Wang, J. Zhang, Z. Li, W. Wu, M. Wu, Alkali halide boost of carbon nitride for photocatalytic H_2 evolution in seawater, ACS Appl. Mater. Interfaces 12 (2020) 48526–48532, https://doi.org/10.1021/acsami.0c13060.

[52] X.-H. Jiang, L.-C. Wang, F. Yu, Y.-C. Nie, Q.-J. Xing, X. Liu, Y. Pei, J.-P. Zou, W.-L. Dai, Photodegradation of organic pollutants coupled with simultaneous photocatalytic evolution of hydrogen using quantum-dot-modified g-c3n4 catalysts under visible-light irradiation, ACS Sustain. Chem. Eng. 6 (2018) 12695–12705, https://doi.org/10.1021/acssuschemeng.8b01695.

[53] S. Zhang, L. Wang, C. Liu, J. Luo, J. Crittenden, X. Liu, T. Cai, J. Yuan, Y. Pei, Y. Liu, Photocatalytic wastewater purification with simultaneous hydrogen production using MoS_2 QD-decorated hierarchical assembly of $ZnIn_2S_4$ on reduced graphene oxide photocatalyst, Water Res. 121 (2017) 11–19, https://doi.org/10.1016/j.watres.2017.05.013.

[54] F. Rao, G. Zhu, W. Zhang, J. Xu, B. Cao, X. Shi, J. Gao, Y. Huang, Y. Huang, M. Hojamberdiev, Maximizing the formation of reactive oxygen species for deep oxidation of NO via manipulating the oxygen-vacancy defect position on $(BiO)_2CO_3$, ACS Catal. 11 (2021) 7735–7749, https://doi.org/10.1021/acscatal.1c01251.

[55] Y. Wu, H. Hu, M. Han, Y. Ouyang, L. Xia, X. Huang, Z. Hu, C. Li, Mechanism insights into the facet-dependent photocatalytic degradation of perfluorooctanoic acid on BiOCl nanosheets, Chem. Eng. J. 425 (2021) 130672, https://doi.org/10.1016/j.cej.2021.130672.

[56] H. Li, J. Shang, H. Zhu, Z. Yang, Z. Ai, L. Zhang, Oxygen vacancy structure associated photocatalytic water oxidation of BiOCl, ACS Catal. 6 (2016) 8276–8285, https://doi.org/10.1021/acscatal.6b02613.

[58] A. Migani, L. Blancafort, What controls photocatalytic water oxidation on rutile TiO$_2$(110) under ultra-high-vacuum conditions? J. Am. Chem. Soc. 139 (2017) 11845–11856, https://doi.org/10.1021/jacs.7b05121.

[59] N. Barbero, D. Vione, Why dyes should not be used to test the photocatalytic activity of semiconductor oxides, Environ. Sci. Technol. 50 (2016) 2130–2131, https://doi.org/10.1021/acs.est.6b00213.

[60] E. Holmström, P. Spijker, A.S. Foster, The interface of SrTiO$_3$ and H$_2$O from density functional theory molecular dynamics, Proc. R. Soc. A-Math. Phys. Eng. Sci., 472 (2016) 20160293. https://doi.org/10.1098/rspa.2016.0293.

[61] G. Yilmaz, T. Yang, Y. Du, X. Yu, Y.P. Feng, L. Shen, G.W. Ho, Stimulated electrocatalytic hydrogen evolution activity of MOF-derived MoS$_2$ basal domains via charge injection through surface functionalization and heteroatom doping, Adv. Sci. 6 (2019) 1900140, https://doi.org/10.1002/advs.201900140.

[62] H. Wang, X. Xiao, S. Liu, C.-L. Chiang, X. Kuai, C.-K. Peng, Y.-C. Lin, X. Meng, J. Zhao, J. Choi, Y.-G. Lin, J.-M. Lee, L. Gao, Structural and electronic optimization of MoS$_2$ edges for hydrogen evolution, J. Am. Chem. Soc. 141 (2019) 18578–18584, https://doi.org/10.1021/jacs.9b09932.

[63] P. Liu, J. Zhu, J. Zhang, P. Xi, K. Tao, D. Gao, D. Xue, P dopants triggered new basal plane active sites and enlarged interlayer spacing in MoS$_2$ nanosheets toward electrocatalytic hydrogen evolution, ACS Energy Lett. 2 (2017) 745–752, https://doi.org/10.1021/acsenergylett.7b00111.